Performance Calculation for a High-Speed Solid-Rotor Induction Motor

Jacek F. Gieras, *Fellow, IEEE*, and Juha Saari

***Abstract*—The paper deals with analytical method of design and prediction of performance characteristics for induction motors with solid steel rotor coated with copper layer. On the basis of the distribution of the 2-D electromagnetic field, the equivalent impedance of the rotor has been derived. The edge effect and nonlinear magnetic permeability of solid steel have been included. The presented analytical method has been verified with laboratory test results. A 300 kW, 60 000-rpm, three-phase solid-rotor induction motor for the next generation air compressor has been investigated. The accuracy of analytical approach is acceptable and can be recommended for rapid design of solid-rotor induction motors.**

***Index Terms*—AC machines, AC motor drives, electromagnetic field, equivalent circuit, high-speed machines, induction motors, performance, solid rotor.**

NOMENCLATURE

a_R, a_X	Coefficients for including nonlinearity and hysteresis losses of ferromagnetic materials.
B	Magnetic flux density, T.
b_ν	Coefficient of Fourier series for B.
d	Thickness, general symbol, m.
d_{Cu}	Thickness of copper layer, m (Fig. 1).
E	Electric field intensity, V/m; electromotive force (EMF), V.
f	Frequency, Hz.
g	Air gap (mechanical clearance), m.
H	Magnetic field intensity, A/m.
h_{2b}	Rotor bar height, m.
I	Electric current, A.
k_{RN}	Edge effect coefficient for copper layer (Russel-Northworthy's factor).
k_{tr}	Coefficient of transformation of the rotor impedance to the stator winding (turns ratio).
k_w	Winding factor.
k_z	Edge effect coefficient for solid steel.
k_ν	Attenuation coefficient of electromagnetic field for the νth harmonic, 1/m.
L	Axial length of the rotor without end zones, m.
N	Number of turns.
P	Active (true) power; power losses, W.
p	Number of pole pairs.
s	Slip.
t_{ov}	Thickness of copper layer behind the stator stack, m.
V	Input phase voltage.
w_{ov}	Length of rotor behind the stator stack, m.
$Z = R + jX$	Impedance, Ω.
$z = r + jx$	Unit impedance, Ω.
$\alpha_\nu = (a_R + ja_X)k_\nu$	Complex propagation constant of electromagnetic field, 1/m.
β_ν	Constant (real number) dependent on pole pitch, 1/m.
$\kappa_\nu = (\alpha_\nu^2 + \beta_\nu^2)^{1/2}$	Complex propagation constant of electromagnetic field dependent on β_ν, 1/m.
σ	Electric conductivity, S/m.
τ	Pole pitch, m.
$\mu_0 = 0.4\pi \times 10^{-6}$	Magnetic permeability of free space, H/m.
$\mu_{re} = \mu_{rs}(\mu' - j\mu'')$	Complex equivalent magnetic permeability.
μ_{rs}	Relative surface magnetic permeability.
ν	Number of space harmonic.
ξ	Reduced height of nonferromagnetic bar.
ω	Angular frequency, rad/s.

Manuscript received January 29, 2011; revised May 9, 2011 and May 27, 2011; accepted June 1, 2011. Date of publication June 23, 2011; date of current version February 10, 2012.

J. F. Gieras is with the Electrical Engineering Department, University of Technology and Life Sciences, 85-796 Bydgoszcz, Poland, and Hamilton Sundstrand Applied Research, Rockford, IL 61125 USA (e-mail: jgieras@ieee.org).

J. Saari was with Sundyne Corporation, 02150 Espoo, Finland. He is now with the Industrial Technology Division, Ingersoll Rand, 02201 Espoo, Finland (e-mail: juhasaari@irco.com).

Color versions of one or more of the figures in this paper are available online at http://ieeexplore.ieee.org.

Digital Object Identifier 10.1109/TIE.2011.2160516

I. INTRODUCTION

THE objective of this paper is twofold:

1) to prove that a solid-rotor induction machine shows good performance as a high-speed motor for the next generation compressors;
2) to provide a fast and efficient analytical tool for designing solid-rotor induction motors in industry.

The most common machine types in high-speed applications are induction machines [4], [7], [9], [11], [14], [20], [26], [28]–[30], [33], [35], [38]. The highest speed of induction motors can be achieved using a solid rotor made of mild steel instead

0278-0046/$26.00 © 2011 IEEE

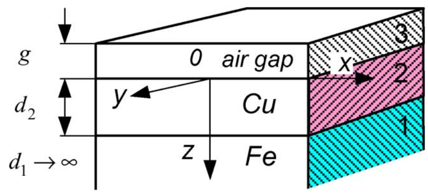

Fig. 1. Layered halfspace for analysis of 2-D electromagnetic field.

of a cage rotor. Although the principle of operation of solid-rotor induction machines is similar to that of other induction machines, the analysis of physical effects in solid rotors on the basis of classical electrodynamics of nonlinear conductive bodies is intricate. Problems arise both due to nonlinearity of solid ferromagnetic bodies and complex structures of certain types of these machines [2], [13], [14], [25], [28], [37]. The electromagnetic field in the rotor is strictly 3-D, even if the rotating magnetic field excited by the stator system can be assumed as 2-D [13], [14]. The performance of the machine depends on the intensity and distribution of vectors of the electromagnetic field, in particular, of the vectors of current density and magnetic flux density [13], [14].

Research in the area of induction machines with solid ferromagnetic rotor was initiated in the 1920s by Russian scientists K. I. Shenfer and J. S. Bruk [14]. In the further years of the 20th century, many researchers and engineers worldwide contributed to the theory and technology of these machines.

Intensive research studies in solid-rotor induction machines have been done in the 1950s through the early 1970s, e.g., fundamental contributions of W. J. Gibbs (1947), H. M. McConnel (1953), A. J. Wood and C. Concordia (1960), G. Angst (1962), J. C. Wilson, R. E. Hopkins and Erdelyi (1965), R. A. Jamieson (1968), L. A. Finzi and D. A. Paice (1968), H. Yee (1971), B. J. Chalmers and Wooley (1972), H. Yee an J. C. Wilson (1972), M. S. Sarma and G. R. Soni (1972), and many other scientists. In the same years, a lot of papers have also been written in Russia and Eastern Europe (Poland, Ukraine, Lithuania, Czechoslovakia). Major contributions worldwide are discussed in [14], where also various geometrical structures of solid rotors have been analyzed.

Concepts of solid-rotor induction motors have been developed in connection with a search for removing drawbacks of cage induction motors in order to achieve:

1) reduction of the inrush starting current;
2) simplification and reduction of costs of manufacture of the rotor;
3) high reliability and high mechanical integrity;
4) low vibration and acoustic noise level (in the case of slotless rotor).

Early potential applications of solid-rotor induction motors included motors for high number of starts and reversals, motors operating at increased slip, induction machines installed in harsh environment, starters for large turboalternators, eddy-current couplings and brakes, torque motors in gyroscopic systems, etc.

Before the vector control era (1970s), there were also attempts to use solid rotors coated with thin copper layer for very small-diameter rotors of two-phase servo motors, in which the cage winding and laminated back iron (yoke) were very difficult to accommodate. Research was also stimulated by trends in developments of other types of electrical machines, e.g., machines with rotors made of soft magnetic powders (magnetodielectrics and dielectromagnetics), shields for end windings of large turbogenerators, shields for superconducting machines, and retaining sleeves for high-speed permanent magnet (PM).

In spite of extensive research in academia, there was practically no interest in solid-rotor induction motors by electrical machine industry between 1950 and 1980.

Solid-rotor induction motors were resurrected in the 1990s in connection with high-speed technology [2]–[4], [9], [12], [18], [20], [22], [23], [25]–[30], [33], [35], [37]. Recent interest in electric machines with alternating electromagnetic field in solid ferromagnetic parts is motivated by new applications of electrical machines as, for example, motors for high-speed direct drive compressors, motors for pumps, motors for drills, superconducting machines, high-speed generators, and bearingless machines [16]–[18], [20], [22], [25]–[30], [33], [35], [36]. Extensive research in the last two decades in the area of high-speed solid-rotor induction machines have been done at Swiss Federal Institute of Technology in Zurich, e.g., [28], Helsinki University of Technology, e.g., [3], [4], and Lappeenranta University of Technology, e.g., [2], [18], [25], [26].

In comparison with cage-rotor induction motors of the same dimensions, solid-rotor induction motors have lower output power, lower power factor, lower efficiency, higher no-load slip, and higher mechanical time constant. Worse performance characteristics are due to:

1) low electric conductivity (in comparison with aluminum and copper alloys) and low saturation magnetic flux density (in comparison with silicon steel and cobalt alloys) of mild steels;
2) large nonferromagnetic air gap between the stator and rotor cores in the case of solid rotor coated with copper layer (high magnetizing current, low power factor);
3) increased eddy-current losses in copper layer and solid-rotor body due to higher harmonics of magnetic field.

In spite of all these drawbacks, the solid rotor is a preferred choice for high-speed induction machines, because its high mechanical integrity allows for achieving the tip speed up to twice the tip speed of an equivalent cage rotor with laminated stack. An alternative choice for high-speed applications can be induction motor with drag-cup rotor [8].

There are wide possibilities of reduction of the rotor impedance that improves the performance characteristics through [14]:

1) selecting the solid material with small relative magnetic permeability-to-electric conductivity ratio (μ_r/σ) and adequate mechanical integrity (tensile strength);
2) using a layered (sandwiched) rotor with both high magnetic permeability and high conductivity materials;
3) using a solid rotor with additional cage winding;
4) using a solid rotor with axial or radial slits.

Sensible application of the above recommendations that leads to optimization of the design is only possible on the basis of the analysis of the electromagnetic field distribution in the machine. Although, the 2-D and 3-D analysis of electromagnetic field in solid ferromagnetic rotors of induction machines was a frequent topic of papers published in the 1950s and 1960s, this problem is still of significant interest, e.g., [16]–[18], [23], [25], [32], [35].

II. Analysis

A. Distribution of Electromagnetic Field

If the distribution of the magnetic flux density normal component on the surface of a double-layer structure Cu–Fe (Fig. 1) is known, i.e.,

$$b(x,t) = \sum_{\nu=1}^{\infty} \left[B_\nu^+ e^{j(\omega_\nu t - \beta_\nu x)} + B_\nu^- e^{j(\omega_\nu t + \beta_\nu x)} \right] \quad (1)$$

where B_ν^+, B_ν^- are magnitudes of the νth harmonics of the forward- and backward-rotating magnetic flux density waves, the 2-D electromagnetic field equations have the following form [13], [14]:

1) for $0 \le z \le d_2$

$$H_{x\nu 2}^{(2)} = (\pm j)\frac{1}{\beta_\nu}\kappa_{\nu 2}\frac{1}{\mu_2}\frac{1}{M_{\nu 2}}B_\nu e^{\mp j\beta_\nu x} \times \left[\frac{\kappa_{\nu 1}}{\kappa_{\nu 2}}\cosh[\kappa_{\nu 2}(z-d_2)] - \frac{\mu_1}{\mu_2}\sinh[\kappa_{\nu 2}(z-d_2)]\right] \quad (2)$$

$$H_{z\nu 2}^{(2)} = \frac{1}{\mu_2}\frac{1}{M_{\nu 2}}B_\nu e^{\mp j\beta_\nu x} \times \left[\frac{\mu_1}{\mu_2}\cosh[\kappa_{\nu 2}(z-d_2)] - \frac{\kappa_{\nu 1}}{\kappa_{\nu 2}}\sinh[\kappa_{\nu 2}(z-d_2)]\right] \quad (3)$$

$$E_{y\nu 2}^{(2)} = j\omega_{\nu 2}\mu_2(\mp j)\frac{1}{\beta_\nu}\frac{1}{M_{\nu 2}}B_\nu e^{\mp j\beta_\nu x} \times \left[\frac{\mu_1}{\mu_2}\cosh[\kappa_{\nu 2}(z-d_2)] - \frac{\kappa_{\nu 1}}{\kappa_{\nu 2}}\sinh[\kappa_{\nu 2}(z-d_2)]\right] \quad (4)$$

2) for $z > d_2$

$$H_{x\nu 1}^{(2)} = (\pm j)\frac{1}{\beta_\nu}\kappa_{\nu 1}\frac{1}{\mu_1}\frac{1}{M_{\nu 2}}B_\nu e^{\mp j\beta_\nu x}e^{-\kappa_{\nu 1}(z-d_2)} \quad (5)$$

$$H_{z\nu 1}^{(2)} = \frac{1}{\mu_1}\frac{1}{M_{\nu 2}}B_\nu e^{\mp j\beta_\nu x}e^{-\kappa_{\nu 1}(z-d_2)} \quad (6)$$

$$E_{y\nu 1}^{(2)} = j\omega_{\nu 1}\mu_1(\mp j)\frac{1}{\beta_\nu}\frac{1}{\mu_1}\frac{1}{M_{\nu 2}}B_\nu e^{\mp j\beta_\nu x} \quad (7)$$

where

$$M_{\nu 2} = \frac{\kappa_{\nu 1}}{\kappa_{\nu 2}}\sinh(\kappa_{\nu 2}d_2) + \frac{\mu_1}{\mu_2}\cosh(\kappa_{\nu 2}d_2) \quad (8)$$

$$W_{\nu 2} = \frac{\mu_1}{\mu_2}\sinh(\kappa_{\nu 2}d_2) + \frac{\kappa_{\nu 1}}{\kappa_{\nu 2}}\cos(\kappa_{\nu 2}d_2). \quad (9)$$

Subscripts "1" and "2" denote the number of layer in Fig. 1, and ν denotes the space harmonic number. It is assumed that the stator magnetic field changes sinusoidally with the frequency $f = \omega/(2\pi)$, and there is only fundamental time harmonic $\nu = 1$. For current-conductive parts (rotor), the complex propagation constant is expressed as

1) for the forward-rotating field B_ν^+

$$\alpha_\nu = \alpha_\nu^+ = \sqrt{j\omega_\nu^+\mu_0\mu_{rs}\sigma} = (a_R + ja_X)k_\nu^+ = (a_R + ja_X)\sqrt{1-\nu(1-s)}\,k \quad (10)$$

2) for the backward-rotating field B_ν^-

$$\alpha_\nu = \alpha_\nu^- = \sqrt{j\omega_\nu^-\mu_0\mu_{rs}\sigma} = (a_R + ja_X)k_\nu^- = (a_R + ja_X)\sqrt{1+\nu(1-s)}\,k. \quad (11)$$

The coefficient a_R takes into account the nonlinear magnetic permeability and hysteresis losses for the resistance. The coefficient a_X takes into account the nonlinear magnetic permeability and hysteresis losses for the reactance. For ferromagnetic bodies $a_R \approx 1.45$, $a_X \approx 0.85$. For paramagnetic or diamagnetic bodies $a_R = a_X = 1$. Detailed considerations are given in earlier works of the first author cited in [14]. Instead of coefficients a_R and a_X, a complex equivalent magnetic permeability $\mu_{re} = \mu_{rs}(\mu' - j\mu'')$ can be introduced, because $\mu' = a_R a_X$ and $\mu'' = 0.5(a_R^2 - a_X^2)$. The concept of equivalent magnetic permeability and elliptical approximation of hysteresis loop is not only used for analysis of solid-rotor induction motors, but also for analysis of current-carrying conductors [1], laminated cores [15], [34], magnetic bearings [21], and magnetic media [32].

Derivation of coefficients a_R and a_X is intricate, but their application is simple. This method of taking into account the nonlinear permeability and hysteresis losses originated by L. R. Neyman [14] is theoretically better justified than, for example, the method of P. D. Agarwal used in the paper [26]. Experimental verification on both solid-rotor induction motors and single-sided linear motors shows also good accuracy and practical usefulness of (10) and (11) in analytical calculations [13], [14].

The attenuation coefficient for a conductive medium with its relative magnetic permeability μ_r and conductivitiy σ is

$$k_\nu = \sqrt{\frac{\omega_\nu\mu_0\mu_r\sigma}{2}}$$

$$\omega_\nu^+ = \sqrt{1-\nu(1-s)}\omega; \quad \omega_\nu^- = \sqrt{1+\nu(1-s)}\omega. \quad (12)$$

For $\nu = 1$ the attenuation coefficient $k_{\nu=1} = k = \sqrt{\omega\mu_0\mu_r\sigma/2}$ and is the reciprocal of the equivalent depth of penetration. The following relationship exists between complex propagation constants α_ν, κ_ν and real constant β_ν

$$\kappa_\nu = \left(\alpha_\nu^2 + \beta_\nu^2\right)^{\frac{1}{2}} = (a_{R\nu} + ja_{X\nu})k_\nu \quad (13)$$

in which

$$a_{R\nu} = \frac{1}{\sqrt{2}}\left\{\left[4a_R^2a_X^2 + \left(a_R^2 - a_X^2 + \frac{\beta_\nu^2}{k_\nu^2}\right)\right]^{\frac{1}{2}} + a_R^2 - a_X^2 + \frac{\beta_\nu^2}{k_\nu^2}\right\}^{\frac{1}{2}} \quad (14a)$$

$$a_{X\nu} = \frac{1}{\sqrt{2}}\left\{\left[4a_R^2a_X^2 + \left(a_R^2 - a_X^2 + \frac{\beta_\nu^2}{k_\nu^2}\right)\right]^{\frac{1}{2}} - a_R^2 + a_X^2 - \frac{\beta_\nu^2}{k_\nu^2}\right\}^{\frac{1}{2}} \tag{14b}$$

$$\beta_\nu = \nu\frac{\pi}{\tau}. \tag{14c}$$

B. Surface Impedance

The surface impedance of the infinitely thick inner layer 1 is equal to the ratio of the tangential electrical component to the tangential magnetic component at $z = d_2$

$$z_{\nu 1}^{(2)} = z_{\nu 1} = \left[\frac{E_{y\nu 1}^{(2)}}{H_{x\nu 1}^{(2)}}\right]_{z=d_2} = \mp\frac{j\omega_{\nu 1}\mu_1}{\kappa_{\nu 1}} = \mp\frac{j\omega_{\nu 1}\mu_1\sigma_1}{\kappa_{\nu 1}}\frac{1}{\sigma_1} = \mp\frac{\alpha_{\nu 1}^2}{\kappa_{\nu 1}}\frac{1}{\sigma_1} \approx \frac{\alpha_{\nu 1}}{\sigma_1}. \tag{15}$$

The surface impedance of layers 1 and 2 is equal to the ratio of the electrical component to tangential magnetic component at $z = 0$, i.e.,

$$z_{\nu 12}^{(2)} = \left[\frac{E_{y\nu 2}^{(2)}}{H_{x\nu 2}^{(2)}}\right]_{z=0} = \mp\frac{j\omega_{\nu 2}\mu_2}{\kappa_{\nu 2}}\frac{\frac{\mu_1}{\mu_2}\cosh(\kappa_{\nu 2}d_2) + \frac{\kappa_{\nu 1}}{\kappa_{\nu 2}}\sinh(\kappa_{\nu 2}d_2)}{\frac{\kappa_{\nu 1}}{\kappa_{\nu 2}}\cosh(\kappa_{\nu 2}d_2) + \frac{\mu_1}{\mu_2}\sinh(\kappa_{\nu 2}d_2)}. \tag{16}$$

After multiplying the numerator and denominator by

$$\frac{j\omega_{\nu 1}}{j\omega_{\nu 1}}\frac{\mu_2}{\mu_1}\frac{1}{\cosh(\kappa_{\nu 2}d_2)}$$

the impedance (16) takes the form

$$z_{\nu 12}^{(2)} = \mp\frac{j\omega_{\nu 2}\mu_2}{\kappa_{\nu 2}}\frac{1 + \frac{j\omega_{\nu 1}\mu_2\kappa_{\nu 1}}{j\omega_{\nu 1}\mu_1\kappa_{\nu 2}}\tanh(\kappa_{\nu 2}d_2)}{\frac{j\omega_{\nu 1}\mu_2\kappa_{\nu 1}}{j\omega_{\nu 1}\mu_1\kappa_{\nu 2}} + \tanh(\kappa_{\nu 2}d_2)} = \mp\frac{j\omega_{\nu 2}\mu_2}{\kappa_{\nu 2}}\frac{1 + \frac{1}{z_{\nu 1}}\frac{j\omega_{\nu 1}\mu_2}{\kappa_{\nu 2}}\tanh(\kappa_{\nu 2}d_2)}{\frac{1}{z_{\nu 1}}\frac{j\omega_{\nu 1}\mu_2}{\kappa_{\nu 2}} + \tanh(\kappa_{\nu 2}d_2)} \tag{17}$$

where $z_{\nu 1}$ is the impedance of the infinitely thick inner layer 1 (halfspace). Thus, the impedance of the outer layer 2 is

$$z_{\nu 2} = \left[z_{\nu 12}^{(2)}\right]_{z_{\nu 1}^{(2)}\to\infty} = \mp\frac{j\omega_{\nu 2}\mu_2}{\kappa_{\nu 2}}\frac{1}{\tanh(\kappa_{\nu 2}d_2)}. \tag{18}$$

If the thickness d_1 of the inner layer 1 is smaller than the equivalent depth of penetration, its impedance is

$$z_{\nu 1} = \mp\frac{j\omega_{\nu 1}\mu_1}{\kappa_{\nu 1}}\frac{1}{\tanh(\kappa_{\nu 1}d_1)}. \tag{19}$$

If $d_1 \to \infty$, the hyperbolic function in the denominator $\tanh(\kappa_{\nu 1}d_1) \to 1$ and $z_{\nu 1} = j\omega_\nu\mu_1/\kappa_{\nu 1}$.

C. Rotor Impedance

If the inner layer 1 is a solid steel and the outer layer 2 is a copper plate, then, for the fundamental harmonic $\nu = 1$, $d_1 = d_{Fe}$, $d_2 = d_{Cu}$, $\mu_1 = \mu_0\mu_{re}$ [13], [14], $\mu_2 = \mu_0$, $\kappa_1 = \kappa_{Fe}$, $\kappa_2 = \kappa_{Cu}$, $\omega_1 = \omega_2 = \omega$. The impedance is

1) for solid steel

$$Z_{Fe} = \frac{j\omega\mu_{Fe}}{\kappa_{Fe}}\frac{1}{\tanh(\kappa_{Fe}d_{Fe})}\frac{L}{\tau} \tag{20}$$

2) for copper layer

$$Z_{Cu} = \frac{j\omega\mu_0}{\kappa_{Cu}}\frac{1}{\tanh(\kappa_{Cu}d_{Cu})}\frac{L}{\tau} \tag{21}$$

where L is the axial length of the solid ferromagnetic core and τ is the pole pitch. The resultant impedance of a double-layer solid rotor is calculated as a parallel connection of Z_{Fe} and Z_{Cu}, i.e.,

$$Z_2 = \frac{Z_{Fe}Z_{Cu}}{Z_{Fe} + Z_{Cu}} = \frac{\frac{j\omega\mu_{Fe}}{\kappa_{Fe}}\frac{1}{\tanh(\kappa_{Fe}d_{Fe})}\frac{j\omega\mu_0}{\kappa_{Cu}}\frac{1}{\tanh(\kappa_{Cu}d_{Cu})}}{\frac{j\omega\mu_{Fe}}{\kappa_{Fe}}\frac{1}{\tanh(\kappa_{Fe}d_{Fe})} + \frac{j\omega\mu_0}{\kappa_{Cu}}\frac{1}{\tanh(\kappa_{Cu}d_{Cu})}}\frac{L}{\tau}. \tag{22}$$

After multiplying the numerator and denominator of the impedance Z_2 according to (22) by

$$\frac{\kappa_{Fe}}{j\omega\mu_{Fe}}\tanh(\kappa_{Cu}d_{Cu})$$

the rotor impedance becomes

$$Z_2 = \frac{j\omega\mu_0}{\kappa_{Cu}}\frac{\frac{1}{\tanh(\kappa_{Fe}d_{Fe})}}{\frac{\kappa_{Fe}}{j\omega\mu_{Fe}}\frac{j\omega\mu_0}{\kappa_{Cu}} + \frac{\tanh(\kappa_{Cu}d_{Cu})}{\tanh(\kappa_{Fe}d_{Fe})}}\frac{L}{\tau} = \frac{j\omega\mu_0}{\kappa_{Cu}}\frac{\frac{1}{\tanh(\kappa_{Fe}d_{Fe})}}{\frac{1}{z_{Fe}}\frac{j\omega\mu_0}{\kappa_{Cu}} + \frac{\tanh(\kappa_{Cu}d_{Cu})}{\tanh(\kappa_{Fe}d_{Fe})}}\frac{L}{\tau}. \tag{23}$$

If $d_{Fe} \to \infty$, the hyperbolic function in the denominator $\tanh(\kappa_{Fe}d_{Fe}) = 1$ and

$$Z_2 = \frac{j\omega\mu_0}{\kappa_{Cu}}\frac{1}{\frac{1}{z_{Fe}}\frac{j\omega\mu_0}{\kappa_{Cu}} + \tanh(\kappa_{Cu}d_{Cu})}\frac{L}{\tau}. \tag{24}$$

The rotor impedance can also be found straightforward from (17), i.e.,

$$Z_2 = \frac{j\omega\mu_0}{\kappa_{Cu}}\frac{1 + \frac{1}{z_{Fe}}\frac{j\omega\mu_0}{\kappa_{Cu}}\tanh(\kappa_{Cu}d_{Cu})}{\frac{1}{z_{Fe}}\frac{j\omega\mu_0}{\kappa_{Cu}} + \tanh(\kappa_{Cu}d_{Cu})}\frac{L}{\tau}. \tag{25}$$

Since

$$\frac{1}{z_{Fe}}\frac{j\omega\mu_0}{\kappa_{Cu}}\tanh(\kappa_{Cu}d_{Cu}) \ll 1 \tag{26}$$

(24) and (25) are equivalent. Introducing the coefficient k_{tr} of transformation of the rotor impedance to the stator winding with N_1k_{w1} effective number of turns per phase, i.e.,

$$k_{tr} = \frac{m_1(N_1k_{w1})^2}{m_2(N_2k_{w2})^2} = \frac{2m_1(N_1k_{w1})^2}{p} \tag{27}$$

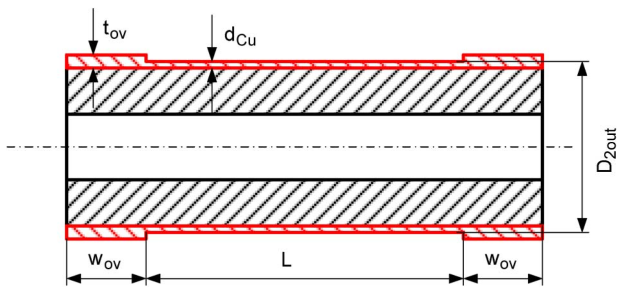

Fig. 2. Solid steel rotor coated with copper layer. To minimize the rotor impedance, the thickness of the copper layer behind the stator stack is thicker than under the stack (US54732111 [3]).

the rotor impedance referred to the stator system is

$$Z_2' = \frac{j\omega\mu_0}{\kappa_{Cu}} \frac{1 + \frac{1}{z_{Fe}}\frac{j\omega\mu_0}{\kappa_{Cu}}\tanh(\kappa_{Cu}d_{Cu})}{\frac{1}{z_{Fe}}\frac{j\omega\mu_0}{\kappa_{Cu}} + \tanh(\kappa_{Cu}d_{Cu})} k_{tr}\frac{L}{\tau}. \quad (28)$$

For a solid-rotor induction machine, the number of rotor phases $m_2 = 2p$, number of rotor turns per phase $N_2 = 0.5$, and rotor winding factor for fundamental harmonic $k_{w2} = 1$.

To include the edge effect [13], [14], [26] the conductivity of solid steel σ_{Fe} in the parameter κ_{Fe} should be multiplied by the reciprocal of the edge effect factor k_z squared, i.e.,

$$\sigma'_{Fe} = \frac{1}{k_z^2}\sigma_{Fe}$$

where [14], [15]

$$k_z = 1 + \frac{2}{\pi}\frac{\tau}{L} \quad (29)$$

and the conductivity of copper layer σ_{Cu} in κ_{Cu} should be multiplied by Russell-Northworthy's coefficient k_{RN} [13], i.e.,

$$\sigma'_{Cu} = k_{RN}\sigma_{Cu} \quad (30)$$

where

$$k_{RN} = 1 - \frac{\tanh(0.5\beta_\nu L)}{0.5\beta_\nu L\left[1 + k_t\tanh(0.5\beta_\nu L)\tanh(\beta_\nu w_{ov})\right]} \quad (31)$$

with the correction factor for t_{ov} [13], [14]

$$k_t = 1 + \frac{1.2(t_{ov} - d_{Cu})}{d_{Cu}}. \quad (32)$$

Dimensions t_{ov} and w_{ov} of the solid rotor coated with copper layer are given in Fig. 2. Using separate edge effect coefficients for the solid steel body (29) and for the copper layer (31) with correction for the end zones (32) increases the accuracy of analytical calculations. It has been proven in [13] and [14]. Accurate analytical approach to edge effects is very important for both homogenous solid rotors and rotors coated with copper layers, independent of the thickness of the copper layer d_{Cu}. The correction factor (32) for end zones has been estimated on the basis of experimental tests [13]. The end effect coefficients for both the solid-steel body (29) and copper layer (31) are equivalent to the required reduction of the electric conductivity due to tangential components of eddy currents in the solid rotor.

TABLE I
SPECIFICATIONS OF INVESTIGATED SOLID-ROTOR INDUCTION MOTOR

Specifications	Unit	Value
Power	kW	300
Voltage (line-to-line)	V	400
Synchronous speed	rpm	60 000
Number of poles		2
Class of insulation		H (180°C)
Stator outer diameter	mm	250
Stator inner diameter	mm	115
Stator stack length	mm	173
Air gap (mechanical clearance)	mm	3
Total length of rotor	mm	315.5

Fig. 3. Solid steel rotor coated with copper layer for a 300-kW, 60 000-rpm induction motor. Courtesy of *Sundyne Corporation*, Espoo, Finland.

The equivalent circuit of the solid-rotor induction motor is discussed in Appendices A and B. In Appendix A, an equivalent circuit corresponding to a classical cage-rotor induction motor has been derived, while in Appendix B, the equivalent circuit for solid rotor is compared with that for a deep-bar rotor.

III. COMPUTATIONS

On the basis of the analysis presented in Section II, a computer program for the design and calculation of performance characteristics has been created. A 300-kW, 60 000-rpm induction motor with solid steel rotor coated with copper layer (Fig. 2) has been investigated. Specifications are listed in Table I.

This motor has been developed by *Sundyne Corporation*, Espoo, Finland. *Sundyne* manufactures high-speed solid-rotor induction motors for air compressors. The solid rotor runs up to 400 m/s, i.e., at twice the tip speed of a cage rotor. The speed limit for this technology is 550 m/s [4]. Fig. 3 shows a solid-steel rotor integrated with two impellers. The copper layer is thicker in the rotor end zones than under the stator stack. The air compressor driven by the 300-kW solid-rotor induction motor is shown in Fig. 4.

Fig. 5 shows the calculated magnetic flux density distribution in the air gap. Since the nonferromagnetic air gap $g + d_{Cu}$ is large (Table I), the effect of the stator slot openings on the distribution of the air gap magnetic flux density is negligible (Fig. 5). Fig. 6 shows the resistances and reactances of the copper layer and solid steel body referred to the stator system. The impedance given by (28) has been separated into impedance of the copper layer and solid steel core, similar to (20) and (21).

Figs. 7 and 8 show the steady-state performance characteristics, i.e., input and output power versus speed (Fig. 7) and torques versus speed (Fig. 8).

Fig. 4. Air compressor driven by a 300-kW, 60 000-rpm induction motor with solid rotor coated with Cu layer. The rotor is shown in Fig. 3. Courtesy of *Sundyne Corporation*, Espoo, Finland.

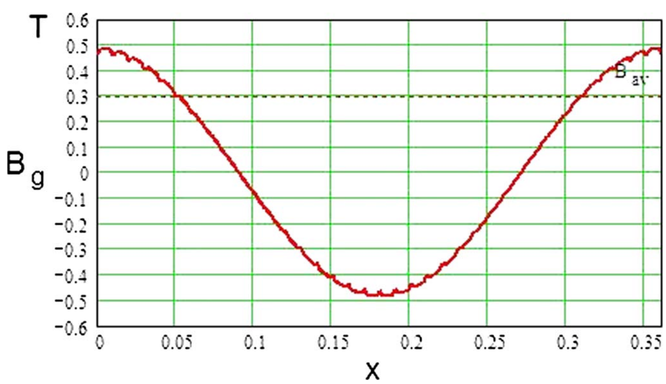

Fig. 5. Distribution of the normal component of the air gap magnetic flux density B_g along the pole pitch. B_{av} = average flux density.

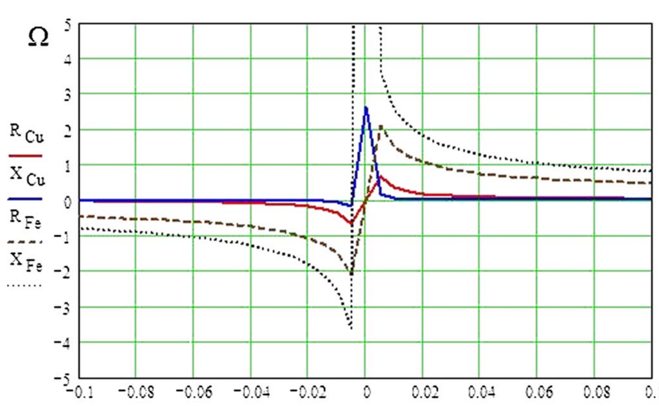

Fig. 6. Resistances and reactances of the Cu layer and solid rotor body referred to the stator winding versus slip at 1000-Hz input frequency.

The electromagnetic power P_{elm} and electromagnetic torque T_{elm} have been calculated in the same way as those for a cage-rotor induction motor, i.e., using the T-type equivalent circuit (Appendix A), in which the rotor nonlinear impedance (dependent on the magnetic permeability of the rotor core) referred to

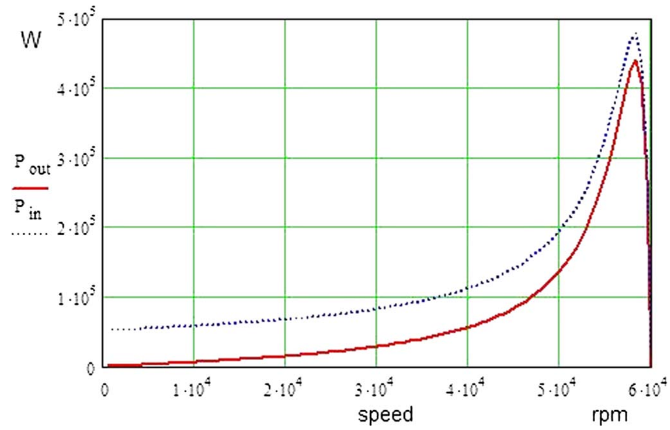

Fig. 7. Output power P_{out} and input power P_{in} versus speed at 400 V and 1000 Hz.

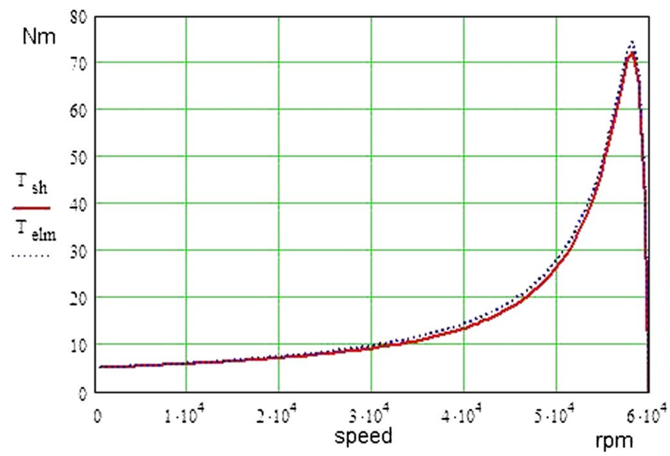

Fig. 8. Shaft torque T_{sh} and electromagnetic torque T_{elm} versus speed at 400 V and 1000 Hz.

the stator winding is expressed by (28). The shaft power has been calculated by subtracting from the electromagnetic power P_{elm} the rotor electrical losses, windage losses, and bearing friction losses.

Since the stator winding has been wound using stranded round wires of small diameter, the eddy-current losses in stator conductors even at the frequency of 1000 Hz are very small. These losses have been approximately included in analytical calculations with the aid of the following skin-effect coefficient for the stator winding resistance

$$k_{1R} \approx 1 + \frac{1}{3}\left(\frac{d_{Cu}}{4\delta_{Cu}}\right)^4 \tag{33}$$

in which d_{Cu} is the diameter of bare wire and δ_{Cu} is the equivalent depth of penetration of the electromagnetic field in the stator conductor. The depth of penetration δ_{Cu} is calculated as the reciprocal of the attenuation coefficient, expressed for the stator winding by similar equation as (12). More details on calculation of losses in stranded conductors due to skin and proximity effects are given in [1], [24], and [31]. Optimal choice for number of strands to minimize eddy-current losses is discussed in [31].

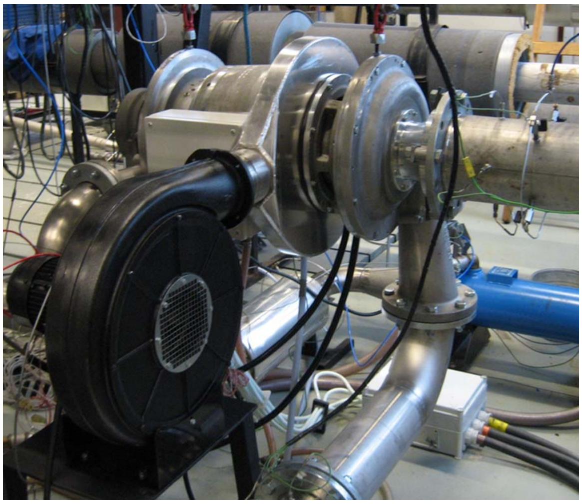

Fig. 9. High-speed compressor with a 300-kW, 60 000-rpm induction motor assembled to the test loop. The stage 1 compressor is on the right and the stage 2 compressor on the left. The unit is cooled by a 3-kW blower (black) shown in the front of the picture.

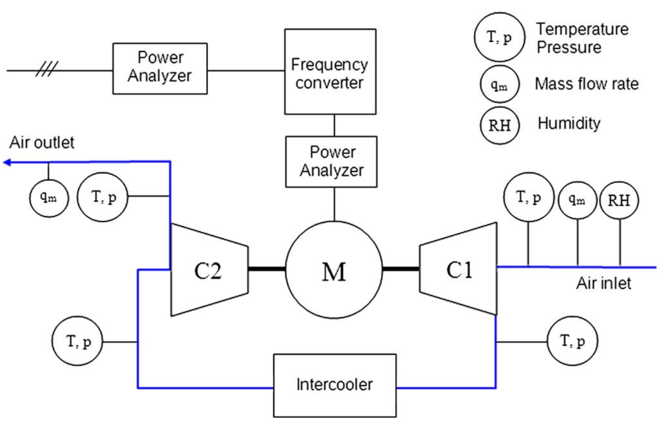

Fig. 10. Test loop block diagram for measurement of the motor and compressor performance.

IV. Laboratory Tests

A 300-kW, 60 000-rpm high-speed solid-rotor induction motor built by *Sundyne Corporation* was tested at Lappeenranta University of Technology, Finland [13]. Specifications including main dimensions of the motor are shown in Table I. The 300-kW induction motor was loaded with a two-stage turbo-compressor connected directly to the motor shaft. The high-speed motor compressor under testing is shown in Fig. 9.

The test loop block diagram and test loop arrangement are presented in Figs. 10 and 11. The air flow is first sucked by the stage 1 and then cooled down before it goes to the stage 2. After discharging from the stage 2, the flow is cooled back to the ambient temperature. The rotor of the motor is integrated with the compressor impellers as shown in Fig. 3.

Fig. 12 shows the power flow chart for the tested motor. In a high-speed machine, the sum of windage and friction losses is of the same order as electric losses. The motor input power is $P_{\rm in}$, the motor mechanical power is $P_{\rm mech}$, and the output power to the compressor stages is $P_{\rm out}$. $P_{\rm el}$ denotes the total electric motor losses (stator winding, stator core [15], [34], rotor, and stray losses), and $P_{\rm wf}$ denotes the windage and friction losses.

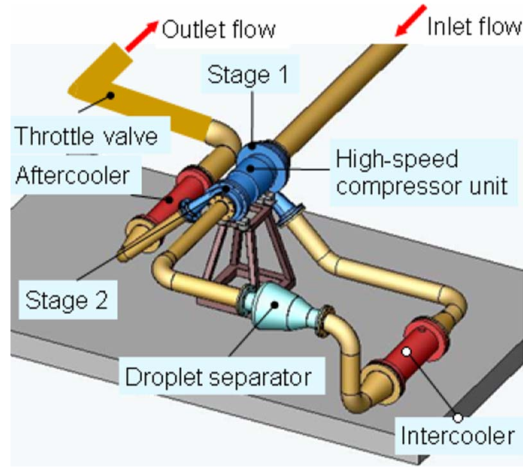

Fig. 11. Test loop arrangement for measurement of the rotor and compressor performance.

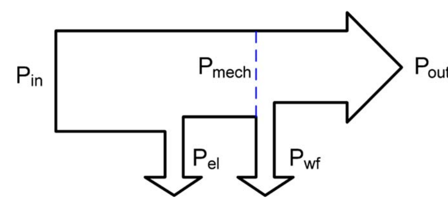

Fig. 12. Simplified power flow chart for a high-speed motor.

The electrical input power of the motor has been measured with the aid of *Norma* power analyzer. The motor phase currents were measured using high band coaxial shunts.

The tested motor has been equipped with active magnetic bearings. The shaft rotational speed has been measured with the aid of a speed sensor connected to the magnetic bearing controller. The supply frequency has been obtained from the frequency converter.

Since compressor impellers are integrated with the rotor of the induction motor, it has not been possible to measure the motor torque directly in a traditional way. Instead, the motor output power has been calculated on the basis of the measured compressor stage performance as

$$P_{out} = \frac{P_1}{\eta_1} + \frac{P_2}{\eta_2} \tag{34}$$

in which P_1 and P_2 are the gas compressor powers for stage 1 and stage 2, respectively, and η_1 and η_2 are the corresponding isentropic efficiencies. All these values can be calculated by measuring the inlet and outlet flow parameters (pressure p, temperature T, humidity RH) as well as the mass flow rate q_m for both stages separately (Fig. 10).

In order to obtain the motor mechanical power, the windage and friction losses P_{wf} must be added to the calculated output power. The windage and friction losses of the machine have been measured by deceleration tests without the compressor impellers. Based on the deceleration time, the windage and friction losses can be calculated from

$$P_{wf} = J\,\Omega \frac{d\Omega}{dt} \tag{35}$$

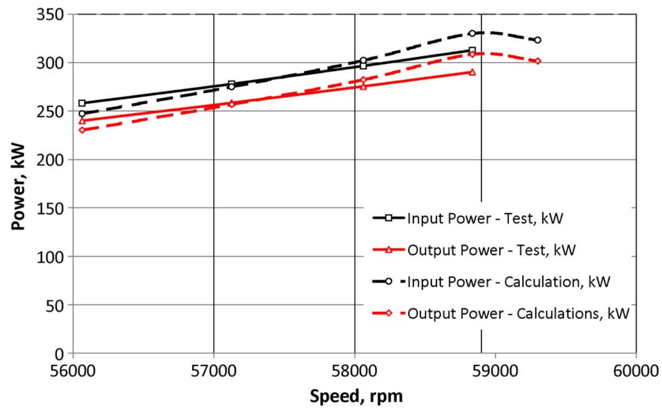

Fig. 13. Input and output power curves versus speed obtained from calculations and measurement for a 300-kW, 60 000-rpm induction motor with solid rotor coated with copper layer at 400 V and variable frequency 942 to 1000 Hz (Table II).

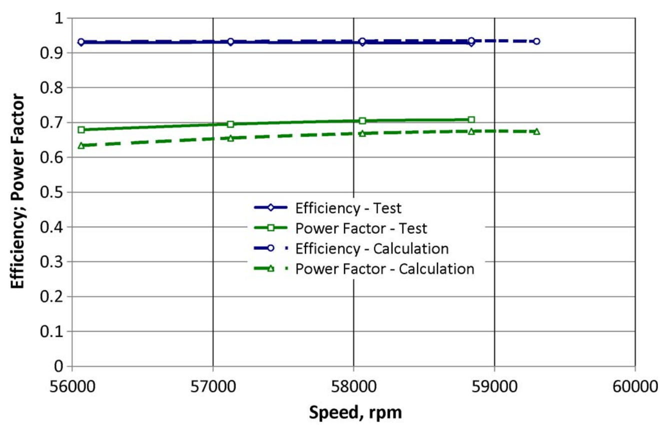

Fig. 14. Efficiency–speed and power factor–speed curves obtained from tests and calculations for a 300-kW, 60 000-rpm induction motor with solid rotor coated with copper layer at 400 V and variable frequency.

where J is the rotor moment of inertia, $\Omega = 2\pi n$ is the shaft angular speed, and t is the time.

The tested motor has been cooled with an air flow forced through the stator winding and the air gap. The required power of the blower is 3.0 kW, which is a relatively small number for a 300-kW motor. A low blower power has been achieved by a careful design of the air cooling paths. In addition, water circulation in the motor housing reduces the needed air cooling. As all the heat produced by the motor losses have been taken out by the cooling air and water, it has been possible to measure the total losses of the motor by a calorimetric method [19]. The obtained results have been in good agreement with the losses calculated on the basis of the electrical input power and output power.

V. Comparison of Calculations with Test Results

Analytical calculations performed according to the presented theory in Section II have been compared with laboratory measurements performed on the 300-kW, 60 000-rpm solid-rotor induction motor (Table I, Figs. 3 and 4).

TABLE II
Speed, Frequency, and Slip Corresponding to Graphs Plotted in Figs. 13 and 14

Rotor speed, rpm	56064	57126	58062	58836	59300
Synchronous speed, rpm	56520	57660	58680	59550	60000
Frequency, Hz	942	961	978	992.5	1000
Slip	0.00807	0.00931	0.011	0.012	0.012
Stator winding temperature, ^{o}C	119	129	140	152	152

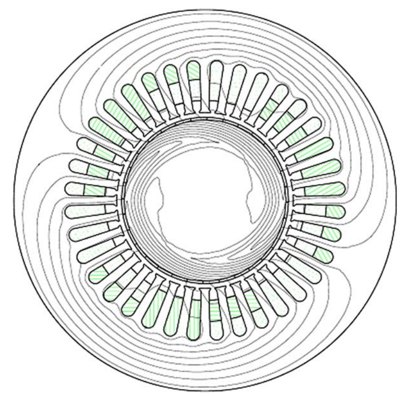

Fig. 15. Magnetic flux distribution in the cross section of the investigated solid-rotor induction motor as obtained from the 2-D FEM.

The input power, output power, efficiency and power factor curves obtained from calculations and laboratory tests are plotted versus speed in Figs. 13 and 14.

The synchronous speed, rotor speed, frequency, slip, and stator winding temperature corresponding to curves plotted in Figs. 13 and 14 are given in Table II. The rotor surface temperature was about 170 °C.

VI. Comparison of Analytical Calculation with the Finite Element Mehod

Finally, the analytical calculations have been compared with those obtained from the FEM. The magnetic field distribution in the cross section of the investigated two-pole solid-rotor induction motor is shown in Fig. 15.

The FEM analysis includes directly only the stator winding losses and rotor losses. The hysteresis and eddy-current losses in the stator core are neglected when solving the magnetic field. These losses have been estimated after the time-stepping simulation from the time variation of the magnetic field. Also, corrections have been made for including the windage and bearing friction losses. Steady-state performance characteristics obtained from the the 3-D FEM and from the presented analytical method have been compared in Figs. 16 and 17.

There is a very good agreement between the FEM and the presented method for the input power, output power, and efficiency. The agreement for power factor is worse, but the difference does not exceed 5%. Discrepancy in power factor is due to low accuracy of calculation of the magnetizing reactance and magnetizing current. Both the magnetizing reactance and magnetizing current have been calculated using classical theory of induction machines.

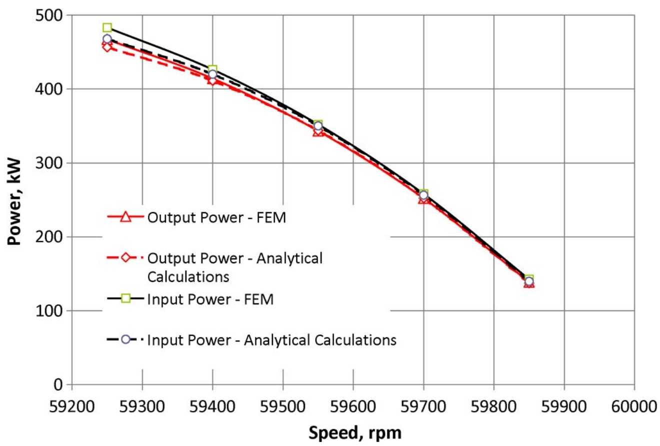

Fig. 16. Input and output power curves versus speed obtained from the 3-D FEM and presented analytical method for a 300-kW, 60 000-rpm induction motor with solid rotor coated with copper layer at 418 V and 1000 Hz.

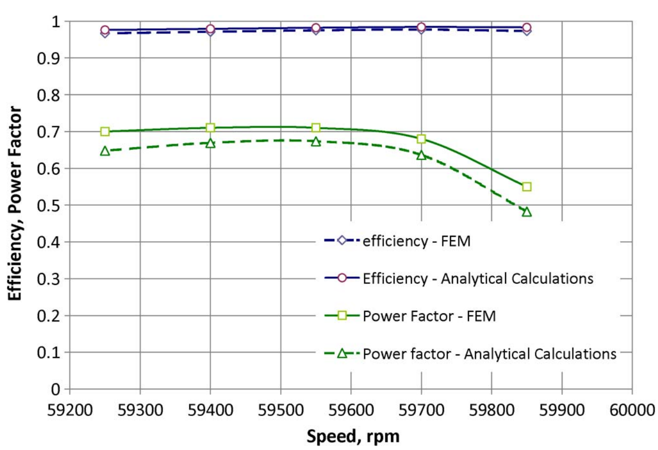

Fig. 17. Efficiency–speed and power factor–speed curves obtained from the 3-D FEM and presented analytical method for a 300-kW, 60 000-rpm induction motor with solid rotor coated with copper layer at 418 V and 1000 Hz.

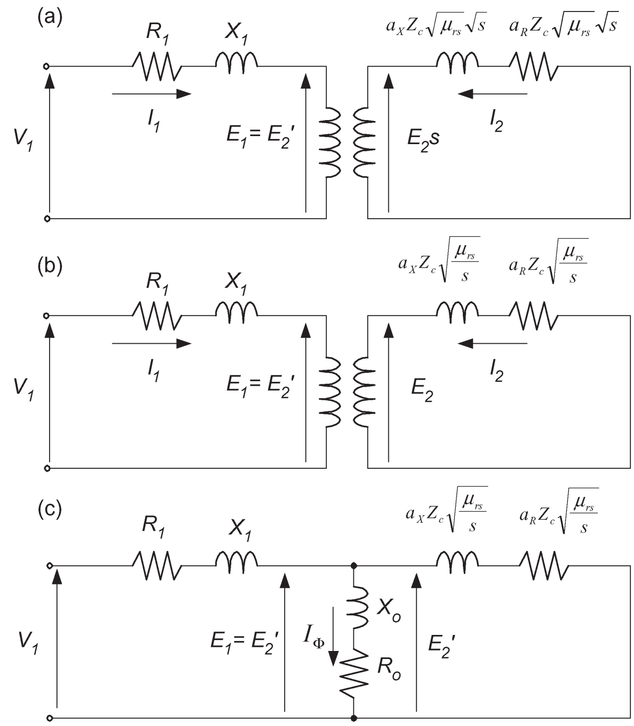

Fig. 18. Equivalent circuits of solid-rotor induction motors: (a) magnetically coupled stator and rotor circuits; (b) magnetically coupled stator and rotor circuit with rotor EMF independent of slip; (c) equivalent circuit of a solid-rotor induction machine as a transformer. The series resistance R_0 represents the stator core losses.

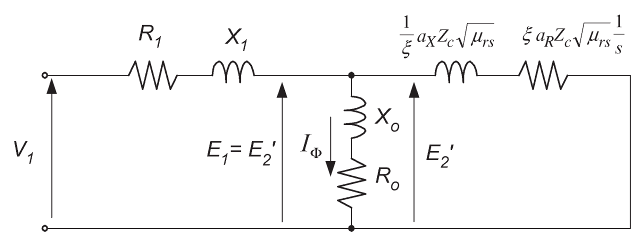

Fig. 19. Equivalent circuit of a solid-rotor induction motor with rotor branch similar to a deep-bar rotor.

The shape of characteristics plotted in Figs. 13 and 14 is different than the shape of characteristics plotted in Figs. 16 and 17, because in the first case, a variable input frequency has been used (Table II), while in the second case, the input frequency $f = 1000\ \text{Hz} = const.$

VII. Conclusion

Although, the approach to the performance calculation of a solid-rotor induction motor is similar to that of a cage induction motor, the electromagnetic effects in a solid ferromagnetic rotor are more complex. The solid-steel core of the rotor conducts both the electric current and magnetic flux, while the copper layer conducts only the electric current. The impedance of the rotor solid steel core depends on the nonlinear magnetic permeability and hysteresis losses. The magnetizing current is high due to the presence of the nonferromagnetic copper layer and high reluctance of the solid steel core [14]. The rotor branch of the equivalent circuit contains the rotor nonlinear resistance and reactance, both dependent on the electric and magnetic parameters of the solid steel and slip (Figs. 18 and 19). The equivalent circuit for a solid-rotor induction motor is not the same as that for a standard induction motor (Appendix A).

Figs. 13 and 14 show that the analytically calculated and measured curves for a 300-kW, 60 000-rpm solid-rotor induction motor are in good agreement. Also, the presented analytical method is in good agreement with the FEM (Figs. 16 and 17).

The solid-rotor induction machine shows good performance as a high-speed induction motor, i.e., it is characterized by small volume envelope, high power density, high efficiency, high starting torque-to-starting current ratio, and high tip speed. Its rigid construction allows for operation at much higher speeds than a cage-rotor induction motor. A solid-rotor induction motor is an excellent candidate as a high-speed motor for the next generation of compressors.

The proposed analytical approach to the design and performance calculation of solid-rotor induction motors based on the 2-D analysis of the electromagnetic field has not worse accuracy than the FEM and is much faster. The created computer program allows for rapid design of solid-rotor induction motors in electrical machine industry.

Appendix A
Equivalent Circuit

For simplicity, only solid rotor without external copper layer ($d_2 = d_{Cu} = 0$), fundamental harmonic $\nu = 1$, and balanced three-phase system will be considered.

For a solid cylinder $d_{Fe} \to \infty$, the hyperbolic function $\tanh(\kappa_{Fe} d_{Fe}) = 1$ and (20) takes the form

$$Z_{Fe} = \frac{j\omega\mu_{Fe}}{\kappa_{Fe}}\frac{L}{\tau} = \frac{j\omega\mu_{Fe}\sigma_{Fe}}{\kappa_{Fe}\sigma_{Fe}}\frac{L}{\tau} \approx \frac{\alpha_{Fe}}{\sigma_{Fe}}\frac{L}{\tau} = (a_R + ja_X)\frac{k_{Fe}}{\sigma_{Fe}}\frac{L}{\tau} \quad (36)$$

where α_{Fe} is according to (10) and (11), κ_ν is according to (13), in which $\nu = 1$ and the attenuation coefficient k_{Fe} for solid steel is according to (12), in which also $\nu = 1$. Thus, including the edge effect [13], [14] with the aid of (29) the impedance of the solid steel rotor is

$$Z_{2s} = (a_R + a_X)k_z\frac{L}{\tau}\sqrt{\frac{\pi s f \mu_0 \mu_{rs}}{\sigma_{Fe}}} \quad (37)$$

where μ_{rs} is the relative magnetic permeability at the surface of ferromagnetic rotor. Typical values of damping coefficients for solid steel rotors with $\tau = 5$ mm, $\mu_{rs} = 100$, $\sigma_{Fe} = 5 \times 10^6$ S/m, $a_R = 1.45$ and $a_X = 0.85$ are: for $f = 50$ Hz, $k_{Fe} = 314.16$ 1/m; for $f = 60$ Hz, $k_{Fe} = 344.14$ 1/m; for $f = 400$ Hz, $k_{Fe} = 888.58$ 1/m; and for $f = 1000$ Hz, $k_{Fe} = 1404.96$ 1/m.

The rotor impedance referred to the stator system is obtained by multiplying the impedance (36) by the coefficient of transformation k_{tr} according to (27), i.e.,

$$Z'_{2s} = (a_R + ja_x)k_{tr}k_z\frac{L}{\tau}\sqrt{\frac{\pi f s \mu_0 \mu_{rs}}{\sigma_{Fe}}} = R'_{2s} + jX'_{2s} \quad (38)$$

$$R'_{2s} = a_R k_{tr} k_z \frac{L}{\tau}\sqrt{\frac{\pi f s \mu_0 \mu_{rs}}{\sigma_{Fe}}} = a_R Z_c \sqrt{\mu_{rs}}\sqrt{s} \quad (39)$$

$$X'_{2s} = a_X k_{tr} k_z \frac{L}{\tau}\sqrt{\frac{\pi f s \mu_0 \mu_{rs}}{\sigma_{Fe}}} = a_X Z_c \sqrt{\mu_{rs}}\sqrt{s} \quad (40)$$

where

$$Z_c = k_{tr} k_z \frac{L}{\tau}\sqrt{\frac{\pi f \mu_0}{\sigma_{Fe}}} \quad (41)$$

is the constant value of the rotor impedance independent of the slip s and surface value of the relative magnetic permeability μ_{rs}.

Assuming the slip-dependent voltage per phase (EMF per phase) that is induced in the rotor as

$$E'_2(s) = 4\sigma_f s f N_2 k_{w2}\Phi\frac{N_1 k_{w1}}{N_2 k_{w2}} = sE'_{20} = sE_{20}\frac{N_1 k_{w1}}{N_2 k_{w2}} = 4\sigma_f s f N_1 k_{w1}\Phi = sE_1 \quad (42)$$

where σ_f is the form factor of the EMF (defined as rms-to-mean value), N_1, N_2 are the numbers of turns of the stator and rotor, respectively, k_{w1}, k_{w2} are winding factors, Φ is the magnetic flux and

$$E_{20} = 4\sigma_f f N_2 k_{w2}\Phi \quad (43)$$

is the induced rotor voltage at $n = 0 (s = 1)$. The rotor current referred to the stator system can be found as

$$I'_2 = \frac{E'_2(s)}{Z'_2} = \frac{sE_1}{\sqrt{(a_R Z_c\sqrt{\mu_{rs}}\sqrt{s})^2 + (a_X Z_c\sqrt{\mu_{rs}}\sqrt{s})^2}} = \frac{E_1}{\sqrt{\left(a_R Z_c\sqrt{\frac{\mu_{rs}}{s}}\right)^2 + \left(a_R Z_c\sqrt{\frac{\mu_{rs}}{s}}\right)^2}} = \frac{E_1}{\sqrt{\left(\frac{R'_2}{s}\right)^2 + \left(\frac{X'_2}{s}\right)^2}} \quad (44)$$

where

$$R'_2 = \frac{R'_{2s}}{s} = a_R Z_c\sqrt{\frac{\mu_{rs}}{s}} \quad (45)$$

$$X'_2 = \frac{X'_{2s}}{s} = a_R Z_c\sqrt{\frac{\mu_{rs}}{s}} \quad (46)$$

are the resistance and reactance in the rotor branch of the equivalent circuit referred to the stator system. Fig. 18 shows the development of the equivalent circuit (transformer analogy) of a solid-rotor induction motor.

Most equivalent circuits for solid-rotor induction motors discussed in the literature [12], [14] are the same as those for typical cage-rotor induction motors [5], [6], i.e., the resistance in the rotor branch is divided by slip s, while the reactance is independent of slip. This is not true. Appendix I shows how the equivalent circuit for a solid-rotor induction motor should be developed and how the resistance and reactance of the rotor branch vary with the slip.

Appendix B

In a deep-bar rotor induction machine with the rotor bar height h_{2b}, the rotor branch contains the following resistance and reactance

$$\frac{R'_2}{s} \approx \frac{\xi R'_{2b} + R'_{2r}}{s} \quad (47)$$

$$X'_2 \approx \frac{3}{2\xi}X'_{2b} + X'_{2r} \quad (48)$$

where R'_{2b}, X'_{2b} are the rotor bar resistance and reactance referred to the stator system, respectively, and R'_{2r} and X'_{2r} are the end ring resistance and reactance referred to the stator system, respectively. The so-called *reduced height* of the non-ferromagnetic bar is

$$\xi \approx h_{2b}\sqrt{\pi\mu_0 s\, f\sigma}. \quad (49)$$

Similar to a deep-bar rotor, the reduced thickness of the equivalent layer at the rotor surface that conducts the current is

$$\xi = \delta_{Fe0}\sqrt{\pi\mu_0\mu_{rs} s f \sigma_{Fe}} \tag{50}$$

where the equivalent depth of penetration of the electromagnetic field into rotor body at zero speed ($s = 1$) is

$$\delta_{Fe0} = \frac{1}{\sqrt{\pi\mu_0(\mu_{rs})_{s=1} f \sigma_{Fe}}}. \tag{51}$$

Assuming $(\mu_{rs})_{s=1} \approx \mu_{rs}$, on the basis of (49) and (50) the reduced thickness of the current-conductive layer is

$$\xi \approx \sqrt{s}. \tag{52}$$

Thus,

$$R'_{2s} = \xi\, a_R\, k_{tr} k_z \frac{1}{\delta_{Fe0}\ \sigma_{Fe}} \frac{L}{\tau} \tag{53}$$

$$X'_{2s} = \frac{1}{\xi} s a_X k_{tr} k_z \frac{1}{\delta_{Fe0}\ \sigma_{Fe}} \frac{L}{\tau}. \tag{54}$$

In further considerations (41) will be used to simplify the notation. The resistance in the rotor branch is inversely proportional to the slip

$$R'_2 = \frac{R'_{2s}}{s} = \xi\, a_R k_{tr} k_z \frac{1}{\delta_{Fe0}\ \sigma_{Fe}} \frac{L}{\tau}\frac{1}{s} = \xi\, a_R Z_c \sqrt{\mu_{rs}} \frac{1}{s} \tag{55}$$

and reactance in the rotor branch has the same form as that in standard cage induction motors, i.e.,

$$X'_2 = \frac{X'_{2s}}{s} = \frac{1}{\xi} a_X k_{tr} k_z \frac{1}{\delta_{Fe0}\ \sigma_{Fe}} \frac{L}{\tau} = \frac{1}{\xi} a_X Z_C \sqrt{\mu_{rs}} \tag{56}$$

so that the rotor current referred to the stator system is equal to the EMF E_1 divided by the rotor branch impedance, i.e.,

$$I'_2 = \frac{E_1}{\sqrt{\left(\xi\, a_R Z_C \sqrt{\mu_{rs}} \frac{1}{s}\right)^2 + \left(\frac{1}{\xi} a_X Z_C \sqrt{\mu_{rs}}\right)^2}}. \tag{57}$$

The alternative equivalent circuit of a solid-rotor induction motor, similar to that of a deep-bar induction motor, is shown in Fig. 19.

If $a_R \approx 1.45$ and $a_R \approx 0.85$ (typical values for solid steel rotors), the coefficient of the solid ferromagnetic rotor for resistance $\xi a_R \approx 1.45\xi$ and for reactance $a_X/\xi = 0.85/\xi$. For a deep-bar rotor, the same coefficients are ξ and $1.5/\xi$. Note, that the nonlinear magnetic permeability and hysteresis losses have been taken into account by coefficients a_R and a_X, the equivalent depth of penetration δ_{Fe} of electromagnetic field into solid steel rotor body is small in comparison with the height of the nonferromagnetic copper or aluminum bar, the electric conductivity of steel is about ten times lower than the conductivity of copper, and about seven times lower than the conductivity of aluminum. In addition, the surface magnetic permability of solid-rotor body $\mu_{rs} \gg 1$ versus $\mu_r \approx 1$ for a nonferromagnetic bar.

ACKNOWLEDGMENT

The authors would like to thank *Sundyne Corporation*, Espoo, Finland for granting permission to publish photographs and specifications of a 300-kW, 60 000-rpm solid-rotor induction motor.

REFERENCES

[1] J. Acero, R. Alonso, L. A. Barragan, and J. M. Burdio, "Magnetic vector potential based model for eddy-current loss calculation in round-wire planar windings," *IEEE Trans. Magn.*, vol. 42, no. 9, pp. 2152–2158, Sep. 2006.

[2] T. Aho, V. Sihvo, J. Nerg, and J. Pyrhonen, "Rotor materials for medium-speed solid-rotor induction motors," in *Conf. Rec. IEEE IEMDC*, Antalya, Turkey, May 3–5, 2007, pp. 525–530.

[3] A. Arkkio, "Asynchronous electric machine and rotor and stator for use in association therewith," U.S. Patent 54 732 111, Dec. 5, 1995.

[4] A. Arkkio, T. Jokinen, and E. Lantto, "Induction and permanent magnet machines for high speed applications," in *Conf. Rec. ICEMS*, Nanjing, China, 2005, pp. 871–876.

[5] A. Boglietti, A. Cavagnino, and M. Lazzari, "Algorithms for the computation of the induction motor equivalent circuit parameters—Pt I," in *Conf. Rec. IEEE IECON*, Orlando, FL, Nov. 10–13, 2008, pp. 2020–2027, [CD-ROM].

[6] A. Boglietti, A. Cavagnino, and M. Lazzari, "Algorithms for the computation of the induction motor equivalent circuit parameters—Pt II," in *Conf. Rec. IEEE IECON*, Orlando, FL, Nov. 10–13, 2008, pp. 2028–2034.

[7] A. Boglietti, A. Cavagnino, A. Tencon, and S. Vaschetto, "Key design aspects of electrical machines for high-speed spindle applications," in *Conf. Rec. IEEE IECON*, Phoenix, AZ, Nov. 7–10, 2010, pp. 1735–1740, [CD-ROM].

[8] O. Bottauscio, F. Casaro, M. Chiampi, S. Giors, C. Maccarrone, and M. Zucca, "High-speed drag-cup induction motors for turbo-molecular pump applications," *IEEE Trans. Magn.*, vol. 42, no. 10, pp. 3449–3451, Oct. 2006.

[9] M. Centner and U. Schaffer, "Optimized design of high-speed induction motors in respect of the electrical steel grade," *IEEE Trans. Ind. Electron.*, vol. 57, no. 1, pp. 288–295, Jan. 2010.

[10] Z. Cerovsky, J. Novak, and M. Novak, "High speed synchronous motor control for electrically driven compressors on overcharged gasoline or diesel engines," in *Conf. Rec. IEEE IECON*, Porto, Portugal, Nov. 3–5, 2009, pp. 1162–1167, [CD-ROM].

[11] M. Couderc, C. Henaux, and B. Nogarede, "Analytical modeling of high speed electrical machines," in *Conf. Rec. IEEE IECON*, Paris, France, Nov. 6–10, 2006, pp. nil5–nill, [CD-ROM].

[12] L. T. Ergene and S. J. Saolon, "Determining the equivalent circuit parameters of canned solid-rotor induction motors," *IEEE Trans. Magn.*, vol. 41, no. 7, pp. 2281–2286, Jul. 2005.

[13] J. F. Gieras, *Linear Induction Drives*. Oxford, U.K.: Clarendon, 1994.

[14] J. F. Gieras, "Solid-rotor induction motors," in *Handbook of Electric Motors*, G. Kliman and H. Tolyiat, Eds., 2nd ed. New York: Marcel Dekker, 2004, sec. 2.5.7 and 4.6.3.

[15] Z. Gmyrek, A. Boglietti, and A. Cavagnino, "Estimation of iron losses in induction motors: Calculation method, results, and analysis," *IEEE Trans. Ind. Electron.*, vol. 57, no. 1, pp. 161–171, Jan. 2010.

[16] S. L. Ho, N. Shuangxia, and W. N. Fu, "A novel solid-rotor induction motor with skewed slits in radial and axial directions and its performance analysis using finite element method," *IEEE Trans. Appl. Supercond.*, vol. 20, no. 3, pp. 1089–1092, Jun. 2010.

[17] Y. Hu, J. Chen, and X. Ding, "Analysis and computation on magnetic field of solid rotor induction motor," *IEEE Trans. Appl. Supercond.*, vol. 20, no. 3, pp. 1844–1847, Jun. 2010.

[18] J. Huppunen, "High-speed solid rotor induction machine," Ph.D. dissertation, Lappeenranta Univ. Technol., Lappeenranta, Finland, 2004.

[19] T. A. Jankowski, F. C. Prenger, D. D. Hill, S. R. O'Bryan, K. K. Sheth, E. B. Brookbank, D. F. A. Hunt, and Y. A. Orrego, "Development and validation of a thermal model for electric induction motors," *IEEE Trans. Ind. Electron.*, vol. 57, no. 12, pp. 4043–4054, Dec. 2010.

[20] J. Kim, J. Jung, and K. Nam, "Dual-inverter control strategy for high-speed operation of EV induction motors," *IEEE Trans. Ind. Electron.*, vol. 51, no. 2, pp. 312–320, Apr. 2004.

[21] D. C. Meeker, A. V. Filatov, and E. H. Maslen, "Effect of magnetic hysteresis on rotational losses in heteropolar magnetic bearings," *IEEE Trans. Magn.*, vol. 40, no. 5, pp. 3302–3307, Sep. 2004.

[22] G. Mogenier, R. Dufour, G. Ferraris-Besco, L. Durantay, and N. Barras, “Identification of lamination stack properties: Application to high-speed induction motors,” *IEEE Trans. Ind. Electron.*, vol. 57, no. 1, pp. 281–287, Jan. 2010.

[23] T. H. Pham, P. F. Wendling, S. J. Salon, and H. Acikgoz, “Transient finite element analysis of induction motor with external circuit connection and electromagnetic coupling,” *IEEE Trans. Energy Convs.*, vol. 14, no. 4, pp. 1407–1412, Dec. 1999.

[24] A. D. Podoltsev, I. Kucheryavaya, and B. B. Lebedev, “Analysis of effective resistance and eddy-current losses in multiturn winding of high frequency magnetic components,” *IEEE Trans. Magn.*, vol. 39, no. 1, pp. 539–548, Jan. 2003.

[25] J. Pyrhonen, J. Nerg, P. Kurronen, and U. Lauber, “High-speed, 8 MW, solid-rotor induction motor for gas compression,” in *Conf. Rec. 18th ICEM*, Vilamoura, Portugal, Sep. 6–9, 2008, pp. 1–6, [CD-ROM].

[26] J. Pyrhonen, J. Nerg, P. Kurronen, and U. Lauber, “High-speed high-output solid-rotor induction-motor technology for gas compression,” *IEEE Trans. Ind. Electron.*, vol. 57, no. 1, pp. 272–280, Jan. 2010.

[27] T. Raminosoa, B. Blunier, D. Fodorean, and A. Miraoui, “Design and optimization of a switched reluctance motor driving a compressor for a PEM fuel-cell system for automotive applications,” *IEEE Trans. Ind. Electron.*, vol. 57, no. 9, pp. 2988–2997, Sep. 2010.

[28] K. Reichert and G. Pasquarella, “High speed electric machines, status, trends and problems,” in *Conf. Rec. IEEE KTH Stockholm Power Tech. Conf.*, Stockholm, Sweden, 1995, pp. 41–49.

[29] M. Schoning and D. Walti, “Modern PWM drives and high speed machines,” in *Conf. Rec. IEEE IEMDC*, Niagara Falls, Canada, May 15–18, 2011, pp. 634–639, [CD-ROM].

[30] W. L. Song, G. B. Kliman, R. N. Johnson, R. A. White, and J. E. Miller, “Novel high-speed induction motor for a commercial centrifugal compressor,” *IEEE Trans. Magn.*, vol. 36, no. 3, pp. 706–713, May/Jun. 2000.

[31] C. R. Sullivan, “Optimal choice for number of strands in a litz-wire transformer winding,” *IEEE Trans. Power Electron.*, vol. 14, no. 2, pp. 283–291, Mar. 1999.

[32] B. Tellini, M. Bologna, and Pelliccia, “Magnetic field diffusion into conducting nonlinear magnetic media,” *IEEE Trans. Magn.*, vol. 41, no. 3, pp. 1112–1117, Mar. 2005.

[33] P. Tsao, M. Senesky, and S. R. Sanders, “An integrated flywheel energy storage system with homopolar inductor motor/generator and high frequency drive,” *IEEE Trans. Ind. Appl.*, vol. 39, no. 6, pp. 1710–1725, Nov./Dec. 2003.

[34] T. M. Wolbank, R. Wohrnschimmel, and H. Hauser, “Transient simulation of lamination material properties in electrical machines,” *IEEE Trans. Ind. Electron.*, vol. 49, no. 3, pp. 607–612, Jun. 2002.

[35] B. M. Wood, C. L. Olsen, G. D. Hartzo, J. C. Rama, and F. R. Szenasi, “Development of an 11 000-r/min 3500-hp induction motor and adjustable speed drive for refinery service,” *IEEE Trans. Ind. Appl.*, vol. 33, no. 3, pp. 815–825, May/Jun. 1997.

[36] S. Yang, “Electromagnetic actuator implementation and control for resonance vibration reduction in miniature magnetically levitated rotating machines,” *IEEE Trans. Ind. Electron.*, vol. 58, no. 2, pp. 611–617, Feb. 2011.

[37] M. E. Zaim, “Non-linear models for the design of solid rotor induction machines,” *IEEE Trans. Magn.*, vol. 35, no. 3, pp. 1310–1313, May 1999.

[38] C. Zwyssig, S. D. Round, and J. W. Kolar, “An ultrahigh-speed, low power electrical drive system,” *IEEE Trans. Ind. Electron.*, vol. 55, no. 2, pp. 577–585, Feb. 2008.

Jacek F. Gieras (M’83–SM’87–F’02) graduated with distinction from the Technical University of Lodz, Lodz, Poland, in 1971. He received the Ph.D. degree in electrical engineering (electrical machines) and Dr. habil. degree (corresponding to D.Sc.) in electrical engineering from the University of Technology, Poznan, Poland, in 1975 and 1980, respectively.

From 1971 to 1998, he pursued his academic career at several universities worldwide including Poland (Technical University of Poznan and Academy of Technology and Agriculture Bydgoszcz), Canada (Queen’s University, Kingston, ON, Canada), Jordan (Jordan University of Sciences and Technology, Irbid, Jordan), and South Africa (University of Cape Town, Cape Town, South Africa). He was also a Central Japan Railway Company Visiting Professor at the University of Tokyo, Tokyo, Japan (Endowed Chair in Transportation Systems Engineering), Guest Professor at Chungbuk National University, Cheongju, Korea, and Guest Professor at University of Rome La Sapienza, Rome, Italy. In 1987, he was promoted to the rank of Full Professor (life title given by the President of the Republic of Poland). Since 1998, he has been affiliated with United Technologies Corporation, most recently with Hamilton Sundstrand Applied Research. In 2007, he also became Faculty Member (Full Professor) of the University of Technology and Life Sciences in Bydgoszcz, Poland. He authored and coauthored 11 books, over 250 scientific and technical papers and holds 30 patents. The most important books are *Linear Induction Motors*, (U.K.: Oxford University Press, 1994), *Permanent Magnet Motors Technology: Design and Applications*, (New York: Marcel Dekker Inc., 1996), 2nd edition 2002, 3rd edition 2010 (Taylor & Francis), *Linear Synchronous Motors: Transportation and Automation Systems*, (Boca Raton, FL: CRC Press LLC, 1999), 2nd edition 2011, *Axial Flux Permanent Magnet Brushless Machines*, (Springer-Kluwer Academic Publishers, Boston-Dordrecht-London, 2004), 2nd edition 2008 (coauthors R.Wang and M.J. Kamper), *Noise of Polyphase Electric Motors*, CRC Press—Taylor & Francis, 2005 (coauthors C. Wang and J. C. Lai), and *Advancements in Electric Machines*, (Springer, Dordrecht-London-New York, 2008). His research areas are electrical machines, drives, electromagnetics, power systems, and railway engineering.

Prof. Gieras is a Hamilton Sundstrand Fellow (United Technologies Corporation, USA), Full Member of International Academy of Electrical Engineering, and member of Steering Committees of numerous international conferences.

Juha Saari graduated from Tampere University of Technology, Tampere, Finland, in 1991 and obtained Ph.D. degree from Helsinki University of Techology (HUT) (Thermal Analysis of High-speed Electrical Machines), Espoo, Finland, in 1998.

In 1992, he joined the project “Development of a high-speed motor” at HUT. From 1997 to 1999, he worked at High Speed Tech, Espoo, Finland as a R&D Manager. From 1999 to 2011, he worked at Sundyne Corporation, Espoo, Finland, as a Project Manager. He has developed a series of solid-rotor induction motors for high-speed air compressors. At present time, he is affiliated with Ingersoll Rand, Industrial Technologies Division, Espoo, Finland. He has authored several articles in the field of high-speed electrical machines. His research area is high-speed electrical machines, particularly induction machines.

Dr. Saari is a Hamilton Sundstrand Fellow (United Technologies Corporation, USA).